Article

Activation of Thoeris antiviral system via SIR2 effector filament assembly

https://doi.org/10.1038/s41586-024-07092-x

Received: 13 February 2023

Accepted: 19 January 2024

Published online: 21 February 2024

Check for updates

Giedre Tamulaitiene[1,4]✉, Dziugas Sabonis[1,4], Giedrius Sasnauskas[1], Audrone Ruksenaite[1], Arunas Silanskas[1], Carmel Avraham[2], Gal Ofir[2,3], Rotem Sorek[2], Mindaugas Zaremba[1]✉ & Virginijus Siksnys[1]✉

To survive bacteriophage (phage) infections, bacteria developed numerous anti-phage defence systems[1–7]. Some of them (for example, type III CRISPR–Cas, CBASS, Pycsar and Thoeris) consist of two modules: a sensor responsible for infection recognition and an effector that stops viral replication by destroying key cellular components[8–12]. In the Thoeris system, a Toll/interleukin-1 receptor (TIR)-domain protein, ThsB, acts as a sensor that synthesizes an isomer of cyclic ADP ribose, 1′′–3′ glycocyclic ADP ribose (gcADPR), which is bound in the Smf/DprA-LOG (SLOG) domain of the ThsA effector and activates the silent information regulator 2 (SIR2)-domain-mediated hydrolysis of a key cell metabolite, NAD^+ (refs. 12–14). Although the structure of ThsA has been solved[15], the ThsA activation mechanism remained incompletely understood. Here we show that 1′′–3′ gcADPR, synthesized in vitro by the dimeric ThsB′ protein, binds to the ThsA SLOG domain, thereby activating ThsA by triggering helical filament assembly of ThsA tetramers. The cryogenic electron microscopy (cryo-EM) structure of activated ThsA revealed that filament assembly stabilizes the active conformation of the ThsA SIR2 domain, enabling rapid NAD^+ depletion. Furthermore, we demonstrate that filament formation enables a switch-like response of ThsA to the 1′′–3′ gcADPR signal.

During evolution, bacteria developed diverse anti-phage defence systems of varying complexity[1–7]. Some of them (for example, type III CRISPR–Cas, the cyclic nucleotide-based anti-phage signalling system (CBASS), the pyrimidine cyclase system for anti-phage resistance (Pycsar) and Thoeris) exhibit a modular arrangement and consist of two components: a sensor that, in response to infection, produces a signalling molecule from nucleotide precursors; and an effector that binds this molecule and impairs key cellular pathways that impede viral replication at a great cost to the infected cell[8–12,16].

The bacterial antiviral defence system Thoeris, identified in more than 2,000 microbial genomes, is composed of two genes, *thsA* and *thsB*, although *thsB* can be present in multiple copies[1]. Recent studies of the Thoeris system from *Bacillus cereus* MSX-D12 have shown that the ThsB protein of the TIR protein family detects phage infection by a yet unknown mechanism and similarly to plant TIR proteins produces gcADPR (1′′–3′ gcADPR)[12–14]. The 1′′–3′ gcADPR acts as a signalling molecule that is recognized by the carboxy-terminal SLOG domain of the ThsA effector protein and triggers NADase activity at the amino-terminal SIR2 domain resulting in NAD^+ depletion and cell death, thereby preventing further spread of phage infection. Although the structure of ThsA has been solved, the mechanism of ThsA activation by 1′′–3′ gcADPR binding remained incompletely understood, as both 1′′–3′ gcADPR-dependent and autoactive ThsA variants were described[12,14].

Dimeric ThsB′ is active in vitro

We have focused on the Thoeris system from *B. cereus* MSX-D12 that encodes ThsA and two ThsB variants[12,13,15] (Fig. 1a). As isolated ThsB protein showed no functional activity in vitro, we isolated ThsB′ protein, which shares only 18% identity to ThsB[15], and characterized it biochemically and structurally (Extended Data Fig. 1a). Size-exclusion chromatography with multi-angle light scattering revealed that unlike monomeric ThsB[15], ThsB′ is a dimer in solution (Extended Data Fig. 1b). In contrast to ThsB, which produces 1′′–3′ gcADPR in the cell only in response to phage infection, but shows no NAD^+ cyclization activity in vitro[12], ThsB′ exhibited moderate NAD^+ and 1,N^6-etheno-NAD (εNAD^+) cyclization activity in vitro, converting a fraction of NAD^+ and εNAD^+ into 1′′–3′ gcADPR or 1′′–3′ gcεADPR, respectively (Fig. 1b and Extended Data Fig. 1c). Standalone ThsA protein is an NADase that hydrolyses NAD^+ by the SIR2 domain; however, its catalytic activity is low[12,15]. Addition of ThsB′ to the ThsA and NAD^+ or εNAD^+ in vitro reactions markedly stimulated NADase activity of ThsA (Fig. 1b,c and Extended Data Fig. 1d). Substitutions in the ThsA SIR2 NADase (N112A) and ThsB′ (E124A) catalytic sites impaired ThsB′-mediated ThsA activation.

To elucidate the structural features of ThsB′, we solved its crystal structure (Fig. 1d and Extended Data Table 1). The ThsB′ subunit is composed of a seven-stranded β-sheet (βA–βG) surrounded by seven α-helices and slightly differs from the canonical TIR domain, which is

[1]Institute of Biotechnology, Life Sciences Center, Vilnius University, Vilnius, Lithuania. [2]Department of Molecular Genetics, Weizmann Institute of Science, Rehovot, Israel. [3]Present address: Department of Molecular Biology, Max Planck Institute for Biology Tübingen, Tübingen, Germany. [4]These authors contributed equally: Giedre Tamulaitiene, Dziugas Sabonis. ✉e-mail: giedre.tamulaitiene@bti.vu.lt; mindaugas.zaremba@bti.vu.lt; siksnys@ibt.lt

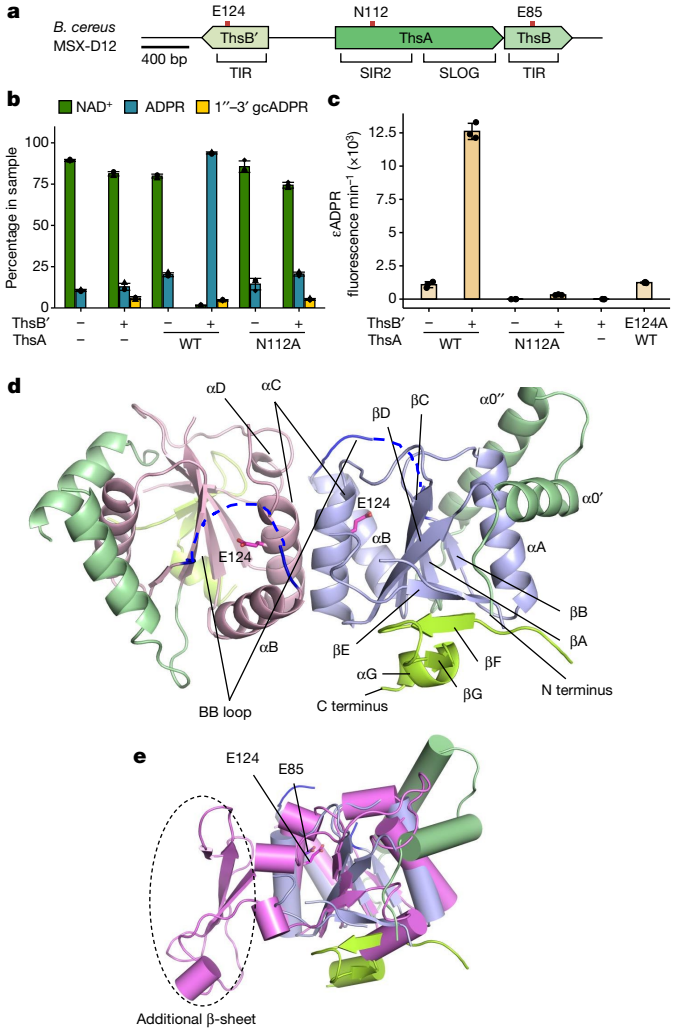

Fig. 1 | Functional and structural features of ThsB′. a, Organization of the *B. cereus* MSX-D12 Thoeris system. Protein domains are indicated. Key catalytic residues of the corresponding proteins are shown. **b**, Liquid chromatography with mass spectrometry of NAD^+ hydrolysis in vitro by ThsB′ and ThsA variants. WT, wild type. **c**, Stimulation of NADase activity of ThsA by ThsB′ in an εNAD^+-based fluorescence assay. In **b**,**c**, data are presented as mean ± s.d. for $n = 3$ independent experiments, with individual data points overlaid. **d**, Crystal structure of the ThsB′ dimer. Monomers are coloured light blue and pink; the BB loop is coloured blue. Unique ThsB′ elements and the N-terminal helices α0′ and α0′′ are coloured light green; the C-terminal βF, βG and αG are coloured lemon green. The catalytic residue E124 is shown in stick representation. **e**, Superposition of ThsB′ with ThsB (PDB ID 6LHY; pink) with their indicated catalytic residues E124 and E85, respectively (DALI[18] *z* score, 7.8; root mean square deviation, 2.8 Å). ThsB′ is coloured as in **d**.

composed of five β-strands and five helices[17] (Fig. 1d and Extended Data Fig. 2a). In the crystal, ThsB′ forms a symmetric dimer involving αB, αC and αD helices (Fig. 1d). Structural superposition of ThsB′ and ThsB (Protein Data Bank (PDB) ID 6LHY) present in the same Thoeris locus revealed a common core, but in ThsB an additional β-sheet is located at the position corresponding to the ThsB′ dimerization interface (Fig. 1e). The top DALI search[18] hit for ThsB′ is 2′-deoxyribosyltransferase (NDT) from the bacterium *Desulfotalea psychrophila*[19] (PDB ID 7O62). The core catalytic unit of NDTs is a dimer and residues from both adjacent subunits contribute to the formation of each binding site[20]. The TIR domain dimer in the activated *Sphingobacterium faecium* STING–di-c-GMP single-fibre structure (PDB ID 7UN8) of the CBASS antiviral defence system exhibits a similar arrangement[21]. The ThsB′ dimer is similar to both NDTs and *S. faecium* STING TIR domain dimers (Extended Data Fig. 2b); however, there is no intersubunit swap of the residues in the NAD^+-binding pocket. Typical TIR domains contain the so-called BB loop (connecting the βB strand and the αB helix), which has been shown to play an important role in signalling by mediating head-to-tail arrangement of the TIR domains[17]. The BB loop of ThsB′ (residues 77–90) is only partially resolved in the electron-density map, indicating its flexibility (Fig. 1d). A flexible BB loop in typical TIR proteins is required for a conformational switch when TIR domains form a TIR filament[22]. The C-terminal part of ThsB′ also differs from other TIR domains, making canonical head-to-tail ThsB′ assembly unlikely; however, it cannot be excluded that alternative higher-order ThsB′ assemblies are formed following phage recognition.

Activated ThsA forms helical filaments

Previous studies suggested that apo-ThsA is either a tetramer or an octamer, and changes its quaternary structure following 1′′–3′ gcADPR binding[12,15]. To monitor ThsA oligomeric state changes in solution, we carried out dynamic light scattering experiments. We found that in the presence of ThsB′ and NAD^+, the wild-type ThsA and N112A SIR2 domain mutant formed large (few micrometre range) particles (Extended Data Fig. 3).

We analysed the structure of these ThsA oligomers using cryo-EM and found that following 1′′–3′ gcADPR binding, the activated ThsA forms long filaments (Fig. 2a). The repeating units of the filament are ThsA tetramers arranged into a regular helical structure with a helical twist of 129.5° and a helical rise of 41.78 Å (Fig. 2b and Extended Data Table 2). The core of the helix is composed of the NADase SIR2 domains, whereas the SLOG domain dimers are pointing away and are not involved in the helical contacts (Supplementary Video 1).

SLOG domain binding of 1′′–3′ gcADPR

In the cryo-EM structure, a 1′′–3′ gcADPR molecule is bound in the predicted pocket of the SLOG domain (Fig. 2c–e). Structural comparison of 1′′–3′ gcADPR-bound SLOG domain dimers with the apo-ThsA crystal structure (PDB ID 6LHX) revealed almost no differences in the overall SLOG domain conformation or relative orientation of the SLOG domains in the dimer (Fig. 2c and Supplementary Video 2); however, it cannot be excluded that domain positions in the available apo-ThsA structure may be affected by crystal packing. Therefore, the details of the structural mechanism of ThsA activation by 1′′–3′ gcADPR remain to be elucidated. 1′′–3′ gcADPR makes multiple contacts with the residues of the SLOG domain similar to those observed in the crystal structure of the isolated SLOG domain–1′′–3′ gcADPR complex[14] (Fig. 2d). In the ThsA helical structure obtained with εNAD^+ instead of NAD^+, the 1′′–3′ gcεADPR resides in the same binding pocket of the SLOG domain as 1′′–3′ gcADPR (Extended Data Fig. 4). The arginine R371, which is crucial for ThsA activation[12], makes contacts with the adenine phosphate and the O4 atom of nicotinamide ribose and buttresses the glutamate E403, which interacts with the 3′ and 2′ OH of nicotinamide ribose. E403A and R371A substitutions compromised oligomerization and the NADase activation in the presence of 1′′–3′ gcADPR (Fig. 2f and Extended Data Fig. 5). Taken together, our results show that 1′′–3′ gcADPR binding by the SLOG domain induces helical filament formation and stimulation of NADase activity of ThsA.

SIR2 active site assembly

The cryo-EM map allows modelling of a fragment of the NAD^+ substrate or the ADPR product in the ThsA SIR2 active site (Fig. 2g–i). The adenine ring of NAD^+ is sandwiched between the side chain of Y266 on one side and G30 and the side chain of M33 on the other side (Fig. 2h). The NAD^+ adenine phosphate makes a single hydrogen bond to the OG atom of

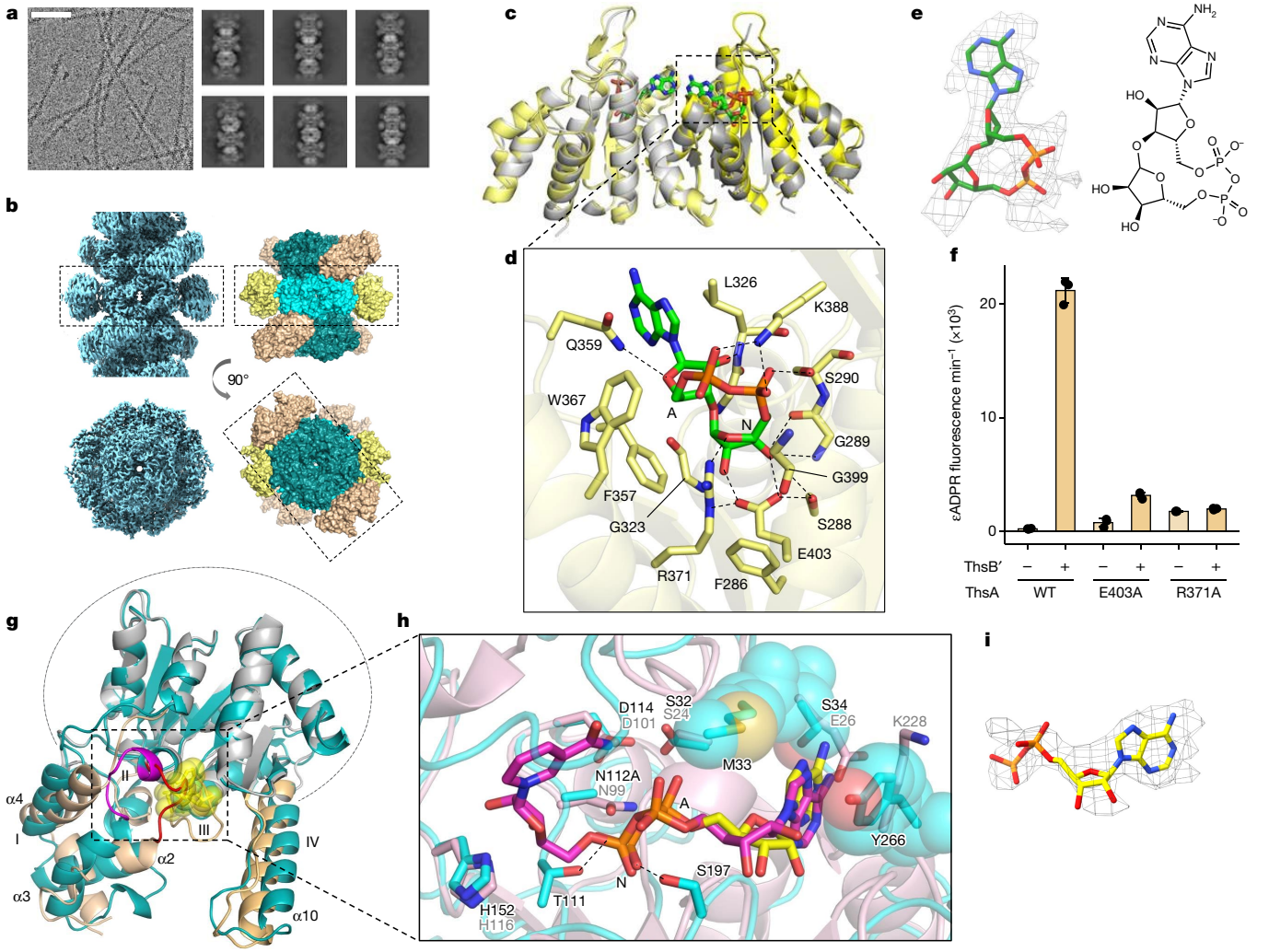

Fig. 2 | Cryo-EM analysis of the activated ThsA. a, Representative micrograph (n = 2,321) and two-dimensional classes of the activated ThsA. Scale bar, 105 nm. **b**, 2.98-Å cryo-EM map of the activated ThsA (left) and a model of the helical filament structure composed of the ThsA tetramers in surface representation (right). The SIR2 domains are coloured cyan; the SLOG domain dimers are shown in yellow. The ThsA tetramer is marked by a rectangle. **c**, 1′′–3′ gcADPR (green) binding in a ThsA SLOG domain dimer (yellow), superimposed with an apo-SLOG domain dimer (grey). **d**, Contacts of 1′′–3′ gcADPR (green) in the ThsA SLOG domain pocket. A and N denote adenine and nicotinamide ribose, respectively. **e**, Local refinement cryo-EM map for 1′′–3′ gcADPR and its chemical formula. **f**, Stimulation of NADase activity of the ThsA SLOG domain mutants by ThsB′ in an εNAD$^+$-based fluorescence assay. Data are presented as mean ± s.d. for n = 3 independent experiments, with individual data points overlaid. **g**, Overlay of apo (6LHX, grey) and activated (cyan) ThsA SIR2 domains. The conserved Rossmann-like fold domain part is encircled. Major conformational differences are observed in regions 33–94 (I, contains helices α2–4), 162–173 (II, helix α7 and N terminus of α8), 196–206 (III, N terminus of α9) and 226–254 (IV, helix α10), coloured light orange in the apo structure. Loop 34–39 is coloured red in the apo structure and magenta in the activated structure. A fragment of NAD$^+$ from the activated structure is shown in yellow. **h**, The SIR2 active site of the activated ThsA (cyan) superimposed with the SIR2 homologue from *Archaeoglobus fulgidus* complexed with NAD$^+$ (1ICI; pink; residue numbers shown in grey). The A and N phosphates of NAD$^+$ are marked. A NAD$^+$ fragment from the ThsA activated structure is coloured yellow; NAD$^+$ from 1ICI is coloured magenta. **i**, Local refinement cryo-EM map of the NAD$^+$ fragment bound in the SIR2 active site.

S197, and the nicotinamide phosphate is contacted by T111, the side chain and the main-chain N atom of S197, and the main-chain N atom of A29. Nicotinamide ribose and nicotinamide rings are not resolved in the map. Superposition of ThsA-bound NAD$^+$ with other NAD$^+$-bound SIR2 protein structures shows a conserved NAD$^+$ position (Fig. 2h).

Structural comparison of the activated ThsA with the apo-ThsA structure indicates major conformational differences in the NADase SIR2 domain that are observed in the elements protruding from the conserved Rossmann-like fold (Fig. 2g). In the apo structure, the loop composed of residues 34–39 blocks the NAD$^+$ access to the active site. In the activated helical filament, this loop moves away, enabling NAD$^+$ binding and catalysis (Fig. 2g,h and Supplementary Video 3). Moreover, in the activated structure, the SIR2 domain slightly rotates with respect to the SLOG domain (Fig. 3a and Supplementary Video 4). This rotation together with the aforementioned conformational changes in the SIR2 domain results in formation of the relatively flat ThsA tetramers that assemble into a helical structure (Fig. 3b and Supplementary Video 5).

ThsA helical interface

In the helical filament each ThsA subunit contacts five other subunits (Extended Data Fig. 6a,b). Both the SLOG and SIR2 domains contribute to the large dimer interface (about 1,900 Å^2), whereas the tetramerization and helical interfaces (about 1,200 Å^2 and about 620–770 Å^2, respectively) are formed only by the SIR2 domains. Many ThsA residues involved in tetramerization and helical filament interfaces reside in the structural elements that differ in conformation in apo and activated ThsA structures (Fig. 2g and Extended Data Fig. 6b). To probe

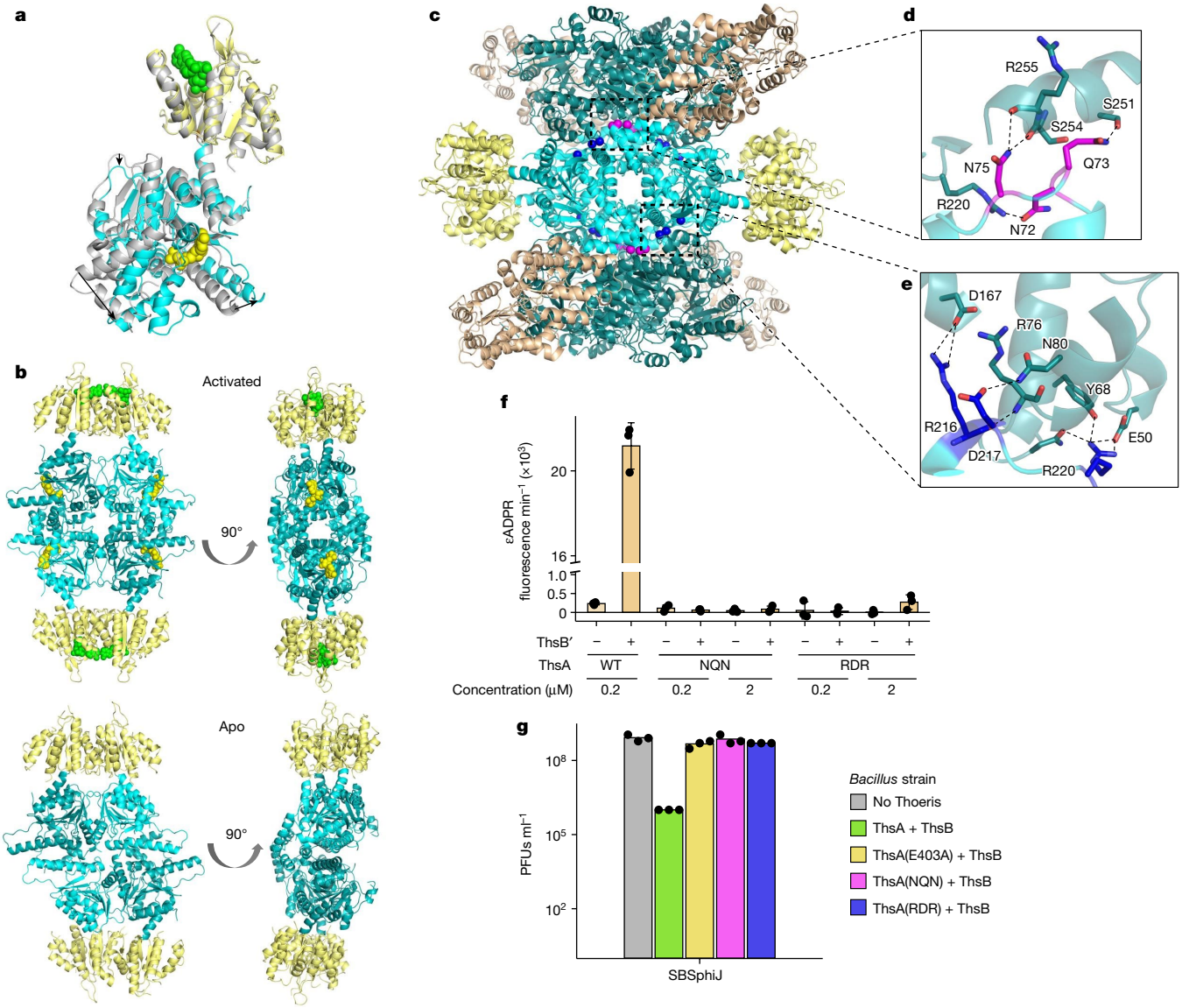

Fig. 3 | Helical filament formation is required for ThsA activation. **a**, Structural overlay of activated ThsA (pale yellow and cyan) with the apo ThsA crystal structure (PDB ID 6LHX; grey) through the SLOG domain. 1′′–3′ gcADPR is shown in green; NAD^+ is shown in yellow. SIR2 domain movement relative to the SLOG domain is indicated by arrows. **b**, Conformational rearrangement of the ThsA tetramer on activation. Note the difference between the asymmetric apo (PDB ID 6LHX) and symmetric activated ThsA tetramers. **c**, The helical interface of ThsA. The CA (α-carbon) atoms of the mutated interface residues are coloured magenta (NQN: N72A/Q73A/N75A) and blue (RDR: R216A/D217A/R220A). **d**,**e**, Details of the NQN (**d**) and RDR (**e**) interfaces. **f**, Stimulation of NADase activity of the ThsA helical interface mutants by ThsB′ in an εNAD^+-based fluorescence assay. **g**, Phage challenge of *Bacillus subtilis* expressing the Thoeris system. The data represent plaque-forming units (PFUs) per millilitre of the phage SBSphiJ infecting cells expressing the Thoeris system with wild-type or mutated ThsA. The data are presented as mean ± s.d. (**f**) and mean (**g**) for $n = 3$ independent experiments, with individual data points overlaid.

the role of the helical filament in ThsA activity, we generated two triple mutants of the helical interface: N72A/Q73A/N75A (NQN) and R216A/D217A/R220A (RDR; Fig. 3c–e). These substitutions had no effect on the secondary and quaternary structure of apo ThsA (Extended Data Fig. 5a,b); however, compromised 1′′–3′ gcADPR triggered formation of higher-order oligomers and ThsA activation (Fig. 3f and Extended Data Fig. 5c), providing direct evidence that helical filament assembly is obligatory for ThsA catalysis. Alterations in the 1′′–3′ gcADPR-binding pocket and helical interface also abolished Thoeris system antiviral defence in *Bacillus* cells (Fig. 3g). This indicates that filament formation is obligatory for Thoeris anti-phage activity in vivo.

We next used the bacterial TIR-domain protein HopAM1 (refs. 14,23) to produce 1′′–3′ gcADPR for further biochemical analysis (Extended Data Fig. 6c). In the presence of the purified 1′′–3′ gcADPR, ThsA formed helical filaments (Extended Data Fig. 6d). We have also determined the dependence of ThsA activity on gcADPR concentration (Fig. 4a). We find that under our experimental conditions, the transition from the background activity level (measured in the absence of 1′′–3′ gcADPR) to the highly active state occurs over a narrow range of gcADPR concentrations in a switch-like manner. Indeed, an increase in 1′′–3′ gcADPR concentration from 1 to 10 nM resulted in an approximately 100-fold acceleration of the 1′′–3′ gcADPR-dependent NADase activity of ThsA (Fig. 4a), indicative of a highly cooperative transition characteristic to high-order assemblies[24–26]. Such a switch-like response to the signalling molecule, occurring at a low nanomolar concentration range, may represent the key benefit of ThsA filament formation. Furthermore, we find that the ThsA filament is highly stable, as it retains nearly full activity after 20 h dialysis against a 1′′–3′ gcADPR-free buffer, and retains most

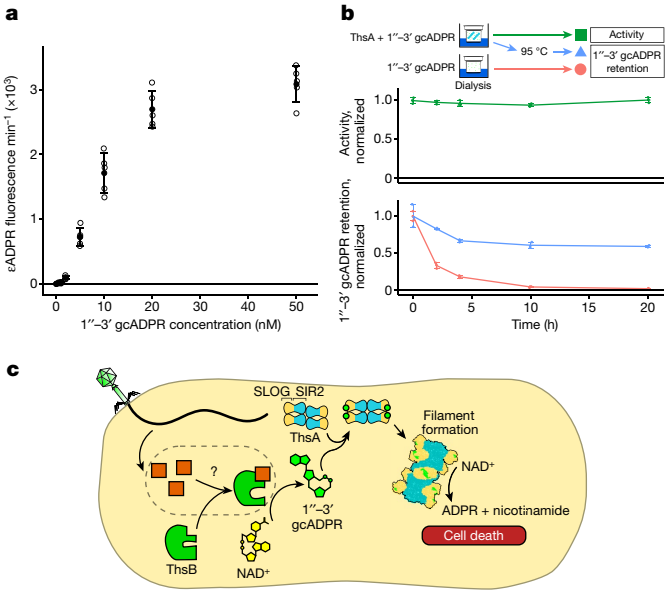

Fig. 4 | ThsA activation by 1′′–3′ gcADPR. a, NADase activity of ThsA in response to 1′′–3′ gcADPR (30 nM ThsA incubated with 100 μM εNAD$^+$ in the presence of 0–50 nM 1′′–3′ gcADPR). The background activity measured in the absence of 1′′–3′ gcADPR was subtracted from each experiment. **b**, ThsA filament stability. NADase activity measurements indicating ThsA–1′′–3′ gcADPR complex activity change and 1′′–3′ gcADPR loss during prolonged dialysis against the 1′′–3′ gcADPR-free buffer. In **a**,**b**, the data are presented as mean (filled dots) ± s.d. for $n = 5$ (**a**) and $n = 3$ (**b**) independent experiments. Individual data points are overlaid (open dots). **c**, Proposed mechanism of action for the Thoeris system.

of the bound 1′′–3′ gcADPR (Fig. 4b). The ThsA SIR2 active site does not cleave the signalling molecule (Extended Data Fig. 6e); thus, once formed, the helical ThsA filament may deplete NAD$^+$ uninterrupted, leading to cell death.

Discussion

On the basis of our combined results, we suggest the following activation mechanism for the Thoeris anti-phage defence system (Fig. 4c): the TIR-domain protein ThsB senses phage infection by an unknown mechanism, becomes activated and produces the signalling 1′′–3′ gcADPR molecule; binding of 1′′–3′ gcADPR by the ThsA SLOG domain leads to the assembly of a helical filament; ThsA filament formation irreversibly activates the SIR2 NADase that depletes NAD$^+$, leading to cell death, thus preventing further spread of phage infection. In this way, Thoeris acts as the last line of antiviral defence that is turned on at the late stages of phage infection, as synthesis of 1′′–3′ gcADPR is observed after 45 min following infection[12], following the failure of all other defence mechanisms.

Although the structures of the ThsA and ThsB proteins are known[15], data on the ThsA activation mechanism are controversial, as both activated and autoactive *B. cereus* ThsA variants have been described[12,14]. Here, using in vitro assays, we show that the catalytic activity of ThsA is regulated through helical filaments that were not detected in previous studies presumably owing to methodological limitations[12,14], although visualization of filament formation in live bacterial cells remains an unresolved challenge. The ThsA SLOG domain serves as the allosteric site that, following gcADPR binding, triggers ThsA oligomerization through the SIR2 domains. This process stabilizes the active conformation of the SIR2 catalytic site, leading to increased NADase activity. Notably, the budding yeast sirtuin Sir2 (NAD$^+$-dependent histone deacetylase) is also allosterically activated by interaction with the structural Sir4 protein that stabilizes two Sir2 domains in a productive conformation[27]. Furthermore, the Sir2–Sir4 interface matches the tetramerization and helical interfaces of the ThsA, implying a conserved SIR2 domain activation and regulation strategy in prokaryotes and eukaryotes (Extended Data Fig. 6f). It remains to be established whether other SIR2-domain-containing proteins including prokaryotic Argonautes[28,29], defence-associated sirtuins[30], AVAST[2] and other systems[4] also form higher-order oligomers that regulate their catalytic activity.

Filament formation has previously been reported for different bacterial antiviral defence systems[10,11,21,31] and eukaryotic innate immunity signal transduction pathways[22,32], but the biological role of such higher-order assemblies remains to be established. Our study of the Thoeris system suggests that filament formation may represent a general strategy to provide a switch-like response to viral infection, allowing an all-or-none reaction, in line with the paradigm of signal transduction in both prokaryotic and eukaryotic cells[24,25]. This type of response enables the cells to avoid self-damage at minimal signalling molecule concentrations, owing to the low residual activity of effector proteins in their low oligomeric state, but grants an immediate switch to the toxic high-order oligomers once the signalling molecule concentration exceeds the threshold level.

Online content

Any methods, additional references, Nature Portfolio reporting summaries, source data, extended data, supplementary information, acknowledgements, peer review information; details of author contributions and competing interests; and statements of data and code availability are available at https://doi.org/10.1038/s41586-024-07092-x.

1. Doron, S. et al. Systematic discovery of antiphage defense systems in the microbial pangenome. *Science* **359**, eaar4120 (2018).
2. Gao, L. et al. Diverse enzymatic activities mediate antiviral immunity in prokaryotes. *Science* **369**, 1077–1084 (2020).
3. Millman, A. et al. An expanded arsenal of immune systems that protect bacteria from phages. *Cell Host Microbe* **30**, 1556–1569 (2022).
4. Rousset, F. et al. Phages and their satellites encode hotspots of antiviral systems. *Cell Host Microbe* **30**, 740–753 (2022).
5. Vassallo, C. N., Doering, C. R., Littlehale, M. L., Teodoro, G. I. C. & Laub, M. T. A functional selection reveals previously undetected anti-phage defence systems in the *E. coli* pangenome. *Nat. Microbiol.* **7**, 1568–1579 (2022).
6. Pingoud, A., Wilson, G. G. & Wende, W. Type II restriction endonucleases — a historical perspective and more. *Nucleic Acids Res.* **44**, 8011–8011 (2016).
7. Koonin, E. V., Makarova, K. S. & Zhang, F. Diversity, classification and evolution of CRISPR-Cas systems. *Curr. Opin. Microbiol.* **37**, 67–78 (2017).
8. Kazlauskiene, M., Kostiuk, G., Venclovas, Č., Tamulaitis, G. & Siksnys, V. A cyclic oligonucleotide signaling pathway in type III CRISPR-Cas systems. *Science* **357**, 605–609 (2017).
9. Niewoehner, O. et al. Type III CRISPR-Cas systems produce cyclic oligoadenylate second messengers. *Nature* **548**, 543–548 (2017).
10. Lowey, B. et al. CBASS immunity uses CARF-related effectors to sense 3′–5′- and 2′–5′-linked cyclic oligonucleotide signals and protect bacteria from phage infection. *Cell* **182**, 38–49 (2020).
11. Tal, N. et al. Cyclic CMP and cyclic UMP mediate bacterial immunity against phages. *Cell* **184**, 5728–5739 (2021).
12. Ofir, G. et al. Antiviral activity of bacterial TIR domains via immune signalling molecules. *Nature* **600**, 116–120 (2021).
13. Leavitt, A. et al. Viruses inhibit TIR gcADPR signalling to overcome bacterial defence. *Nature* **611**, 326–331 (2022).
14. Manik, M. K. et al. Cyclic ADP ribose isomers: production, chemical structures, and immune signaling. *Science* **377**, eadc8969 (2022).
15. Ka, D., Oh, H., Park, E., Kim, J.-H. & Bae, E. Structural and functional evidence of bacterial antiphage protection by Thoeris defense system via NAD+ degradation. *Nat. Commun.* **11**, 2816 (2020).
16. Athukoralage, J. S. & White, M. F. Cyclic nucleotide signaling in phage defense and counter-defense. *Annu. Rev. Virol.* **9**, 451–468 (2022).
17. Nimma, S. et al. Structural evolution of TIR-domain signalosomes. *Front. Immunol.* **12**, 784484 (2021).
18. Holm, L. DALI and the persistence of protein shape. *Protein Sci.* **29**, 128–140 (2020).
19. Fernández-Lucas, J. et al. Biochemical and structural studies of two tetrameric nucleoside 2′-deoxyribosyltransferases from psychrophilic and mesophilic bacteria: Insights into cold-adaptation. *Int. J. Biol. Macromol.* **192**, 138–150 (2021).
20. Armstrong, S. R., Cook, W. J., Short, S. A. & Ealick, S. E. Crystal structures of nucleoside 2-deoxyribosyltransferase in native and ligand-bound forms reveal architecture of the active site. *Structure* **4**, 97–107 (1996).

21. Morehouse, B. R. et al. Cryo-EM structure of an active bacterial TIR–STING filament complex. *Nature* **608**, 803–807 (2022).
22. Martin, R. et al. Structure of the activated ROQ1 resistosome directly recognizing the pathogen effector XopQ. *Science* **370**, eabd9993 (2020).
23. Eastman, S. et al. A phytobacterial TIR domain effector manipulates NAD^+ to promote virulence. *New Phytol.* **233**, 890–904 (2022).
24. Kagan, J. C., Magupalli, V. G. & Wu, H. SMOCs: supramolecular organizing centres that control innate immunity. *Nat. Rev. Immunol.* **14**, 821–826 (2014).
25. Zhang, Q., Bhattacharya, S. & Andersen, M. E. Ultrasensitive response motifs: basic amplifiers in molecular signalling networks. *Open Biol.* **3**, 130031 (2013).
26. Park, C. K. & Horton, N. C. Structures, functions, and mechanisms of filament forming enzymes: a renaissance of enzyme filamentation. *Biophys. Rev.* **11**, 927–994 (2019).
27. Hsu, H.-C. et al. Structural basis for allosteric stimulation of Sir2 activity by Sir4 binding. *Genes Dev.* **27**, 64–73 (2013).
28. Zaremba, M. et al. Short prokaryotic Argonautes provide defence against incoming mobile genetic elements through NAD^+ depletion. *Nat. Microbiol.* **7**, 1857–1869 (2022).
29. Koopal, B. et al. Short prokaryotic Argonaute systems trigger cell death upon detection of invading DNA. *Cell* **185**, 1471–1486 (2022).
30. Garb, J. et al. Multiple phage resistance systems inhibit infection via SIR2-dependent NAD+ depletion. *Nat. Microbiol.* **7**, 1849–1856 (2022).
31. Hogrel, G. et al. Cyclic nucleotide-induced helical structure activates a TIR immune effector. *Nature* **608**, 808–812 (2022).
32. Clabbers, M. T. B. et al. MyD88 TIR domain higher-order assembly interactions revealed by microcrystal electron diffraction and serial femtosecond crystallography. *Nat. Commun.* **12**, 2578 (2021).

Methods

Cloning and mutagenesis

All PCR reactions were carried out using Phusion polymerase (Thermo Fisher catalogue No. F530L) unless otherwise noted. Restriction digest ligation was carried out using T4 DNA ligase (Thermo Fisher catalogue No. EL0011). The *B. cereus* MSX-D12 *thsA* gene (wild type (WT), or encoding N112A or R371A mutants; GenBank accession number EJR09240.1, hypothetical protein II9_05448) was amplified from the pGO9_pAB151_cereus_ThsA_strep plasmid[12] using the primers DS25 and DS26, then cut with EcoRI and inserted into pET-His10_MBP_TEV vector cut with Bsp68I and EcoRI (Thermo Fisher catalogue Nos. ER0111 and ER0271, respectively). All other *thsA* mutants were generated using Phusion polymerase following the manufacturer's protocol using the primers DS58–DS67. The *thsB′* gene (GenBank accession number EJR09239.1, hypothetical protein II9_05447) was cloned with C-terminal TwinStrep-tag into the pAB151 backbone as described before[12]. From this plasmid, the *thsB′* gene was amplified using the primers DS57 and DS53, cut with HindIII (Thermo Fisher catalogue No. ER0501) and inserted into the pET-His_TEV vector backbone amplified using the primers gs-1805 and gs-1804 and cut with HindIII. The E124A ThsB′ mutant was generated using Phusion polymerase following the manufacturer's protocol using the primers DS68 and DS69. Ligation and assembly products were transformed into competent *Escherichia coli* DH5α cells. Plasmids from selected clones were isolated using GeneJET columns (Thermo Fisher catalogue No. K0503) and their sequences were verified by Sanger sequencing. HopAM1 with the C-terminal His-tag gene was synthesized and inserted into the pTK120 vector (Twist Bioscience). The primers used for cloning and mutagenesis are listed in Supplementary Table 1. Bacterial strains and plasmids are listed in Supplementary Table 2.

Protein expression and purification

E. coli BL21 (DE3) cells were transformed with ThsA (WT or mutant), ThsB′ (WT or mutant), ThsB or HopAM1 expression plasmids. Cells were grown at 37 °C in LB medium until the optical density at 600 nm (OD_{600nm}) reached 0.6–0.8; then protein expression was induced with 0.5 mM final isopropyl-β-D-thiogalactoside concentration (or 0.2% final L-arabinose concentration for HopAM1 expression) and cells were grown overnight at 16 °C. The cells were collected by centrifugation, and pellets were resuspended in purification buffer (20 mM Tris-HCl (pH 8.0 at 25 °C), 500 mM NaCl, 5 mM 2-mercaptoethanol, 25 mM imidazole, 2 mM phenylmethylsulfonyl fluoride supplemented with 5% (v/v) glycerol) and lysed by sonication. After removing cell debris by centrifugation, the supernatant was loaded on a Ni^{2+}-charged HiTrap chelating HP column (Cytiva) and eluted with a linear gradient of increasing imidazole concentration (from 25 to 500 mM) in purification buffer supplemented with 5% (v/v) glycerol. Fractions with the protein of interest were pooled and imidazole was removed using a HiPrep 26/10 Desalting column (Cytiva) with purification buffer. The N-terminal tag with a TEV site was cleaved by overnight incubation with TEV protease at 8 °C. Next, the reaction mixture was loaded again onto the Ni^{2+}-charged HiTrap chelating HP column (Cytiva) and the flow-through with pure protein was collected. To purify TwinStrep-tagged ThsB′, cell pellets were resuspended in purification buffer with 5% (v/v) glycerol and disrupted by sonication. Cell debris were removed by centrifugation; then the supernatant was loaded onto a Strep-Tactin XT Superflow column (IBA) and the bound protein was eluted with 50 mM D-biotin solution in purification buffer. Fractions with the protein of interest were pooled, concentrated up to 5 ml using an Amicon Ultra-15 centrifugal filter unit (Merck Millipore) and loaded on a HiLoad 16/600 Superdex 200 gel filtration column (Cytiva) equilibrated with purification buffer. Peak fractions containing the protein of interest were pooled. In the case of HopAM1 protein, the cell lysate was prepared in purification buffer containing 1 M NaCl, subjected to purification using a HiTrap chelating HP column, purified using a Strep-Tactin XT Superflow column, cleaved with TEV protease, concentrated and purified through gel filtration using purification buffer containing 1 M NaCl. All purified proteins were either dialysed against buffer containing 20 mM Tris-HCl (pH 8.0 at 25 °C), 500 mM NaCl, 2 mM dithiothreitol (DTT) and 50% (v/v) glycerol and stored at −20 °C (ThsB′ variants, ThsB and HopAM1) or flash-frozen in liquid nitrogen and stored at −80 °C (ThsA variants). The final protein concentrations were determined by measuring absorbance at 280 nm using sequence-predicted extinction coefficients. The SDS gel of the purified proteins is presented in Extended Data Fig. 1a; uncropped gel images can be found in Supplementary Fig. 1.

Crystallization and structure determination of ThsB′

ThsB′ (with N-terminal His-tag) crystals were obtained by the sitting-drop vapour diffusion method from 15 mg ml^{-1} protein solution in concentration buffer (20 mM Tris-HCl (pH 8.0 at 25 °C), 250 mM NaCl, 2 mM DTT) mixed with an equal amount of reservoir solution (20% (w/v) polypropylene glycol monomethyl ether (PEGMME) 2000, 0.1 M MOPS-HEPES (pH 7.5 at 25 °C), 5% (v/v) glycerol) at 20 °C. The crystals were soaked in cryo-protecting solution (15% PEGMME 2000, 30% PEGMME 550, 0.1 M Na-MES (pH 6.5 at 25 °C)) and flash-cooled for data collection at 100 K. The X-ray diffraction dataset (3.1 Å resolution) was collected at the European Molecular Biology Laboratory–Deutsches Elektronen-Synchrotron PETRA III P14 beamline (Germany) at 0.976300 Å wavelength (100 K) using mxCuBE (v2) software. XDS (v10 January 2022)[33], SCALA (v3.3.22) and TRUNCATE (CCP4 v7.0.000)[34] were used for data processing. The data collection and refinement statistics are presented in Extended Data Table 1. The ThsB′ model was generated using AlphaFold2 (ref. 35) under the ColabFold[36] framework using default parameters and MMseqs2 for homologue search, and used as a template for molecular replacement in Phaser (v2.8.3)[37]. Manual rebuilding of the model was carried out in COOT[38] and the structure was refined with phenix.refine (phenix-1.19.2-4158)[39] with good Ramachandran statistics (97.48% favoured, 2.52% allowed). The final model contains residues 1–16, 25–78, 89–113, 116–163 and 172–192 of the A subunit and 1–78, 87–143, 147–150, 154–164 and 170–192 of the B subunit. The molecular graphics figures were prepared with PyMOL (v2.3.0, The PyMOL Molecular Graphics System, Schrödinger).

LC–MS analysis of NAD^+ reaction products

To determine reaction products of ThsB′ with various substrates, reactions containing 5 μM ThsB′ and 100 μM substrate (NAD^+, εNAD^+ (Sigma catalogue No. N2630)) were prepared in reaction buffer (10 mM HEPES (pH 7.5 at 25 °C), 150 mM NaCl, 5 mM $MgCl_2$, 1 mM DTT) and incubated at 25 °C for 1 h. To determine NADase activity of ThsA in the presence of 1′′–3′ gcADPR, reactions containing 6.66 μM ThsB′ and 133 μM NAD^+ were prepared in reaction buffer and incubated at 25 °C for 1 h. Then, 0.8 μM ThsA (WT or mutants) solution in the same buffer was added in a 1:3 volume ratio to the final concentration of 0.2 μM ThsA or ThsA, 5 μM ThsB′ and 100 μM NAD^+, and further incubated for 30 min before stopping the reaction with a 1:1 phenol/chloroform mixture. For data representation, 260-nm absorbance detector signal chromatogram peak areas were calculated, and the corresponding values were divided by the analyte's extinction coefficient (NAD^+ 18,000, ADPR 15,640, cADPR isomer 15,640 l mol^{-1} cm^{-1}). The obtained values were normalized, so that their sum represents 100%. To determine whether 1′′–3′ gcADPR is cleaved by ThsA, reactions containing 2 μM ThsA and 4 μM 1′′–3′ gcADPR were prepared and incubated at 25 °C for 24 h and analysed by HPLC.

A 1290 Infinity HPLC system (Agilent Technologies) coupled to a 6520 Accurate Mass Q-TOF LC–MS mass analyser (Agilent Technologies) with an electrospray ion source was used for LC–MS analysis. HPLC was carried out on a Supelco Discovery HS C18 column at a temperature of 30 °C. Chromatography was carried out at a 0.3 ml min^{-1} flow rate using a linear mobile phase gradient over 30 min (for positive ionization, 0.02% formic acid in water to 0.02% formic acid in acetonitrile;

for negative ionization, 5 mM ammonium acetate (pH 7.0 at 25 °C) in water to 5 mM ammonium acetate (pH 7.0 at 25 °C) in methanol). MS was carried out using gas at 300 °C, 10 l min^{-1} gas flow, 2,500 V capillary voltage, 150 V fragmentator voltage. Data acquisition and analysis were carried out using QTOF Acquisition Software (B.02.01 SP1) and MassHunter (vB.05.00, Agilent Technologies) software. The experiments were carried out three times.

Production and purification of 1′′–3′ gcADPR

For 1′′–3′ gcADPR production, 10 μM HopAM1 and 1 mM NAD^+ were mixed in reaction buffer and incubated at 37 °C for 1 day. Reaction products were separated using an ÄKTA FPLC (GE) equipped with a Symmetry 100-Å 3.5-μm C18 column (Waters). Chromatography was carried out using a linear mobile phase gradient of phase A (0.1 M triethylamine acetate pH 7.0 in water) and phase B (0.1 M triethylamine acetate pH 7.0 in 60% acetonitrile water solution). The product peak was identified by comparison with the NAD^+ chromatogram, and corresponding fractions were collected, concentrated, lyophilized and stored at −20 °C. The product was verified by LC–MS (Extended Data Fig. 6c).

NADase activity fluorescent assay

The NADase activity of ThsA was assessed using an εNAD^+-based fluorescence assay, in which enzymatic hydrolysis of the εNAD nicotinamide glycosidic bond causes the product εADPR to produce a fluorescent signal. Reactions (60 μl) in reaction buffer containing 100 μM εNAD^+ (Sigma catalogue No. N2630) and 0.2 μM (or 2 μM) ThsA (WT or mutant) and/or 0.5 μM ThsB′ variants were prepared in a 96-well transparent flat-bottom plate (Greiner catalogue No. 655101) and loaded into a CLARIOstar Plus (BMG LABTECH) plate reader, in which fluorescence was measured using 300 nm excitation and 410 nm emission wavelengths in intervals of 1 min or 20 s using orbital scanning and averaging of eight measurements at 25 °C. The reaction rate was determined using linear regression on the linear part of the initial reaction curve in R (v4.0.2) software[40]. As N- or C-terminal expression tags have no influence on ThsB′ activity, all experiments were carried out using ThsB′ with the C-terminal TwinStrep-tag.

To estimate ThsA response to the ligand, 15 μl of 120 nM ThsA was mixed with 15 μl of 0–4 μM 1′′–3′ gcADPR and incubated for 5 min at room temperature, and reaction was initiated with 30 μl 200 μM εNAD^+.

The experiments were carried out 3–5 times as indicated in the figure legends.

Dialysis of ThsA–1′′–3′ gcADPR complex

A 100 μl volume of the sample containing 360 nM ThsA and 360 nM 1′′–3′ gcADPR or only 360 nM 1′′–3′ gcADPR was loaded into a soaked 10 kDa MwCO Slide-A-Lyser MINI Dialysis Unit (Thermo Fisher catalogue No. 69572) and dialysed against 50 ml of reaction buffer. The contents were sampled at 0, 2, 4, 10 and 20 h time points coupled with dialysis buffer change. To evaluate whether 1′′–3′ gcADPR remained bound during dialysis, a portion of the samples was denatured for 5 min at 95 °C. The NADase activity of the dialysed samples was tested in reactions containing 100 μM εNAD^+ and analysed by fluorescent assay. ThsA was added to 30 nM final concentration to the samples containing only 1′′–3′ gcADPR. Three independent experiments were carried out.

Circular dichroism spectroscopy

Concentrations of 0.1 mg ml^{-1} of ThsA protein samples were prepared in a buffer containing 10 mM potassium phosphate (pH 7.5 at 25 °C) and circular dichroism spectra were recorded at 25 °C using a J-815 circular dichroism spectropolarimeter (Jasco) using Spectra Manager (v1.54.03) software.

Size-exclusion chromatography with multi-angle light scattering

Size-exclusion chromatography with multi-angle light scattering of ThsB′ protein variants, C-terminal-tagged ThsB and ThsA (WT and mutants) was carried out at room temperature using a Superdex 200 Increase 10/300 GL column (Cytiva) pre-equilibrated with buffer (20 mM HEPES (pH 7.5 at 25 °C), 250 mM NaCl, 5 mM $MgCl_2$, 1 mM DTT), at 0.4 ml min^{-1} flow rate. A 200-μl sample of 5 μM protein was loaded onto the column. The light-scattering signals were monitored on a miniDawn TREOS II detector; concentrations of protein samples were measured using an Optilab T-rEX refractive index detector (Wyatt Technologies). Data were analysed in Astra software (Wyatt Technologies) using a d*n*/d*c* value of 0.185 ml g^{-1}.

Dynamic light scattering

A 10-μl sample containing 5 μM of ThsA (WT or mutant) and 5 μM ThsB′ was prepared in reaction buffer. Reaction was initiated by adding NAD^+ to a final concentration of 100 μM (only for WT and N112A ThsA) or 2.5 mM. Controls without ThsA, NAD^+ or ThsB′ were also prepared. Sample was loaded into a 2 Microlitre Quartz Cuvette (Malvern Panalytical) and measurements were carried out with a Zetasizer μV photometer (Malvern Panalytical) using Zetasizer Software (v6.20). Measurements were carried out in 1-min runs containing six 10-s measurements. Each run produced a *z*-average value, corresponding to the harmonic-intensity-averaged particle diameter, which was plotted over time.

For endpoint measurements, a 10-μl sample containing 5 μM of ThsA and 5 μM of 1′′–3′ gcADPR was prepared in reaction buffer. Measurements were carried out in 1-min runs containing six 10-s measurements with 30 runs in total.

Phage strains, isolation and cultivation

Phage SBSphiJ was propagated by infecting, at a multiplicity of infection of 0.1, a liquid culture of *B. subtilis* BEST7003 grown at 25 °C to OD_{600nm} of 0.3 in MMB until culture collapse. The culture was then centrifuged for 10 min at 3,200*g* and the supernatant was filtered through a 0.22-μm filter to remove remaining bacteria and bacterial debris.

ThsA mutant transformation and plaque assays

Transformation of Thoeris mutants to the *B. subtilis amyE* locus was carried out using MC medium as described previously[1]. SBSphiJ phage titre was determined using the small drop plaque assay method[41]. A 400 μl volume of overnight culture of bacteria was mixed with 0.5% agar and 30 ml MMB and poured into a 10 cm square plate followed by incubation for 1 h at room temperature. Then, 10-μl drops from tenfold serial dilutions of phage lysate in MMB were dropped on top of the bacterial layer. After the drops dried up, plates were incubated at 30 °C overnight. Plaque-forming units were determined by counting the derived plaques, and lysate titre was determined by calculating plaque-forming units per millilitre. When no individual plaques could be identified, a faint lysis zone across the drop area was considered to be ten plaques. The efficiency of plating (EOP) was measured by comparing plaque assay results on control bacteria and bacteria expressing the Thoeris system.

Cryo-EM sample preparation

ThsA (N112A) buffer was exchanged into buffer containing 20 mM HEPES (pH 7.5 at 25 °C), 150 mM NaCl, 5 mM DTT using illiustra NAP-5 columns (Cytiva) using the manufacturer's protocol, and the protein was concentrated to 2 mg ml^{-1} using an Amicon Ultra 10 kDa centrifuge filter (Merck catalogue No. UFC501096). ThsB′ buffer was exchanged into buffer containing 20 mM Tris-HCl (pH 8.0 at 25 °C), 250 mM NaCl, 2 mM DTT using the same procedure and concentrated. First, 2 mg ml^{-1} ThsB′ and 2 mM NAD^+ or εNAD^+ were incubated at 37 °C for 30 min. Then 2 mg ml^{-1} ThsA was added in a 1:1 volume ratio to a final volume of 20 μl and incubated at 37 °C for 1 h. WT ThsA in the same buffer (1 mg ml^{-1}) was mixed with 1′′–3′ gcADPR (1:1 molar ratio) and incubated at 37 °C for 1 h. The ThsA–ThsB′–NAD^+ (sample I), εNAD^+ (sample II) reaction or ThsA–1′′–3′ gcADPR complex (sample III) (3 μl) was applied

to freshly glow-discharged copper 300 mesh R1.2/1.3 holey carbon grids (Quantifoil), in a Vitrobot Mark IV (FEI) at 4 °C with a waiting time of 0 s and a blotting time of 5 s under 95% humidity conditions. The grids were plunge-frozen in liquid ethane cooled at liquid nitrogen temperature.

Cryo-EM data collection, processing and model building

Cryo-EM data for sample I (dataset I), sample II (dataset II) and sample III were collected using a Glacios microscope (Thermo Fisher Scientific), running at 200 kV and equipped with a Falcon 3EC Direct Electron Detector in electron counting mode (Vilnius University, Vilnius, Lithuania). Images were recorded with EPU (v2.14.0) at a nominal magnification of ×92,000, corresponding to a calibrated pixel size of 1.10 Å per pixel, using exposure of 0.82 electrons $Å^{-2}$ s^{-1}, in 30 frames and a final dose of 30.64 electrons $Å^{-2}$, over a defocus range of −1.0 to −2.0 µm (Extended Data Table 2 and Extended Data Figs. 7 and 8). For dataset I, motion correction was carried out in Relion 3 (ref. 42); then the micrographs were imported to CryoSPARC[43] and patch CTF estimation and micrograph curation were carried out. For dataset II, patch motion correction, CTF estimation and micrograph curation were carried out in real time in CryoSPARC Live[43] (v3.4.0). Further data processing was carried out using standard CryoSPARC[43] (v3.4.0).

For ThsA in the presence of NAD^+, the first set of particles was picked using a filament tracer, and after two-dimensional (2D) classification, templates were generated for template picking. A total of 952,542 particles were picked using a template picker and extracted (box size 320 pixels) from 2,321 accepted micrographs (Extended Data Fig. 7). After 2D classification, the selected particles (233,008) were subjected to ab initio reconstruction and determination of helical parameters. Four copies of the ThsA monomer from the apo crystal structure (PDB ID 6LHX[15], chain A) were fitted into the initial helical refinement map in UCSF ChimeraX[44] (v1.3) indicating D_2 symmetry. Helical parameters (helical twist 128.947°; helical rise 41.870 Å) and D_2 symmetry were used for the final helical refinement job (global resolution, 3.03 Å). In the helical refinement map, the quality of the map for the SLOG domains was much worse than for the central SIR2 domains. To improve map quality, we used 3D no-align classification in Relion 3 (ref. 42) with the mask covering two neighbouring SLOG domains (five classes, $T = 100$) and selected particles of two classes with the highest resolution (194,418 pct). The selected particles were used for local refinement in CryoSPARC[43] with a mask of ThsA monomer (global resolution 3.17 Å). The model of the ThsA monomer (modelled residues 1–342 and 346–476, 1′′–3′ gcADPR and part of NAD^+) was obtained after several rounds of manual inspection and correction in Coot[38] and refinement using phenix.real_space_refine[39] (v1.19.2-4158) against the local resolution map, in which density for the SLOG domain and 1′′–3′ gcADPR was better resolved than in the helical refinement map. As the ThsA NADase mutant N112A was used for the structure determination, we assume that the fragment bound in the SIR2 active site is a part of the substrate NAD^+ and not the product ADPR. Twelve ThsA subunit copies were fitted into the helical refinement map using UCSF ChimeraX[44], clashes between the subunits were resolved in Coot and the final assembly was refined using phenix.real_space_refine (only rigid and ADP refinement).

For dataset II, the particles were picked using the template from dataset I and extracted using a 320-px box (4,644,031 pct; Extended Data Fig. 8). After 2D classification, 935,056 particles were selected and used in helical refinement with D_2 symmetry, initial volume and helical parameters from dataset I (global resolution 2.79 Å). After 3D classification in CryoSPARC[43] (five classes, mask for SLOG domain dimer), two classes were selected (552,570 pct). The local refinement map was obtained using the selected particles and a ThsA monomer mask (global resolution 2.86 Å). The model of the ThsA monomer (modelled residues 2–342 and 345–476, 1′′–3′ gcεADPR and part of εNAD^+) was obtained after several rounds of manual inspection and correction in Coot[38], and refinement using phenix.real_space_refine[39] (v1.19.2-4158) against the local resolution map. Then 12 ThsA subunit copies were fitted into the helical refinement map in UCSF ChimeraX, clashes between the subunits were resolved in Coot and the final assembly was refined using phenix.real_space_refine[39] (only rigid and ADP refinement). Map quality was evaluated using 3DFSC (v3.0).

The statistics of the 3D reconstruction and model refinement are summarized in Extended Data Table 2. The molecular graphics figures were prepared with UCSF ChimeraX[44] (v1.3) and PyMOL (v2.3.0, The PyMOL Molecular Graphics System, Schrödinger). Videos were prepared with UCSF ChimeraX. Protomer contacts were analysed using by PDBePISA[45].

Reporting summary

Further information on research design is available in the Nature Portfolio Reporting Summary linked to this article.

Data availability

All data are available in the manuscript and the Supplementary Information. The atomic coordinates and structure factors or cryo-EM density maps have been deposited in the PDB and Electron Microscopy Data Bank under accession codes 8BTN (ThsB′ crystal structure); 8BTO and EMD-16233 (ThsA–1′′–3′ gcADPR); and 8BTP and EMD-16234 (ThsA–1′′–3′ gcεADPR). The crystal structures in Fig. 1e (PDB accession code 6LHY), 2g and 3a (6LHX) and Fig. 2h (1ICI) and Extended Data Fig. 2b (7O62, 7UN8) and 6f (4IAO) are publicly available from the PDB. Source data are provided with this paper.

Code availability

No code was used for this study.

33. Kabsch, W. *XDS*. *Acta Crystallogr. D* **66**, 125–132 (2010).
34. Collaborative Computational Project, Number 4. The CCP4 suite: programs for protein crystallography. *Acta Crystallogr. D* **50**, 760–763 (1994).
35. Jumper, J. et al. Highly accurate protein structure prediction with AlphaFold. *Nature* **596**, 583–589 (2021).
36. Mirdita, M. et al. ColabFold: making protein folding accessible to all. *Nat. Methods* **19**, 679–682 (2022).
37. McCoy, A. J. et al. Phaser crystallographic software. *J. Appl. Crystallogr.* **40**, 658–674 (2007).
38. Emsley, P. & Cowtan, K. Coot: model-building tools for molecular graphics. *Acta Crystallogr. D* **60**, 2126–2132 (2004).
39. Liebschner, D. et al. Macromolecular structure determination using X-rays, neutrons and electrons: recent developments in Phenix. *Acta Crystallogr. D* **75**, 861–877 (2019).
40. R Core Team. *R: A Language and Environment for Statistical Computing* (R Foundation for Statistical Computing, 2020).
41. Mazzocco, A., Waddell, T. E., Lingohr, E. & Johnson, R. P. in *Bacteriophages* Vol. 501 (eds Clokie, M. R. J. & Kropinski, A. M.) 81–85 (Humana, 2009).
42. Zivanov, J. et al. New tools for automated high-resolution cryo-EM structure determination in RELION–3. *eLife* **7**, e42166 (2018).
43. Punjani, A., Rubinstein, J. L., Fleet, D. J. & Brubaker, M. A. cryoSPARC: algorithms for rapid unsupervised cryo-EM structure determination. *Nat. Methods* **14**, 290–296 (2017).
44. Pettersen, E. F. et al. UCSF ChimeraX: structure visualization for researchers, educators, and developers. *Protein Sci.* **30**, 70–82 (2021).
45. Krissinel, E. Crystal contacts as nature's docking solutions. *J. Comput. Chem.* **31**, 133–143 (2010).
46. Min, J., Landry, J., Sternglanz, R. & Xu, R.-M. Crystal structure of a SIR2 homolog–NAD complex. *Cell* **105**, 269–279 (2001).
47. Morehouse, B. R. et al. STING cyclic dinucleotide sensing originated in bacteria. *Nature* **586**, 429–433 (2020).

Acknowledgements The research has been supported by the Research Council of Lithuania grant S-MIP-21-6 to G.T. The synchrotron X-ray diffraction data were collected at beamline P14 operated by the European Molecular Biology Laboratory, Hamburg at the PETRA III storage ring (Deutsches Elektronen-Synchrotron, Hamburg, Germany). Access to the beamline has been supported by iNEXT-Discovery, project number 871037, funded by the Horizon 2020 programme of the European Commission. We thank I. Drulyte and A. Carabias for discussions on cryo-EM structure determination.

Author contributions G.T. and M.Z. designed the research; D.S. and G.O. cloned the proteins and carried out mutagenesis; A.S. carried out the protein purifications; G.S. and G.T. prepared

cryo-EM samples, collected cryo-EM data, solved the structures and carried out structure analyses; G.T. and D.S. collected X-ray diffraction data, G.T. solved X-ray structure; D.S. carried out biochemical experiments and crystallized ThsB′; A.R. carried out MS analysis; C.A. carried out phage plaque assays; G.T., D.S., G.S., M.Z., R.S. and V.S. wrote the manuscript with input from all authors. All authors read and approved the final manuscript.

Competing interests R.S. is a scientific cofounder of and adviser for BiomX and Ecophage. All other authors declare no competing interests.

Additional information

Supplementary information The online version contains supplementary material available at https://doi.org/10.1038/s41586-024-07092-x.

Correspondence and requests for materials should be addressed to Giedre Tamulaitiene, Mindaugas Zaremba or Virginijus Siksnys.

Peer review information *Nature* thanks Laura Spagnolo and the other, anonymous, reviewer(s) for their contribution to the peer review of this work. Peer reviewer reports are available.

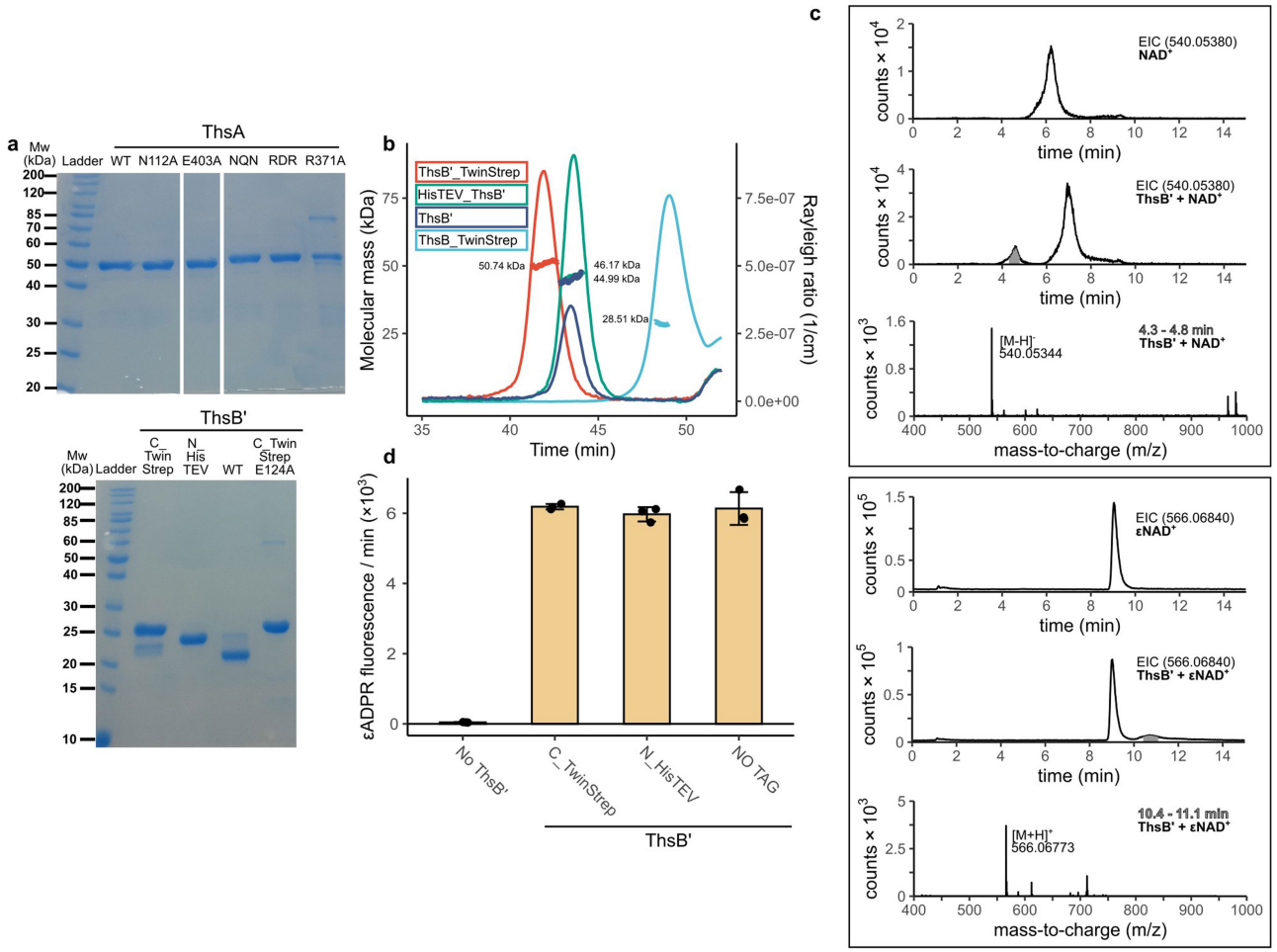

Extended Data Fig. 1 | Characterization of ThasA and ThsB′ proteins. **a**, SDS-PAGE of ThsA and ThsB′ proteins used in this study. Lane images cropped for clarity. A representative gel of n = 2 independent experiments is shown. For gel source data, see Supplementary Fig. 1. **b**, Size-exclusion chromatography with multi-angle light scattering analysis tagged and non-tagged ThsB′ indicates that ThsB′ exists as a dimer. Theoretical weights of the dimers are: ThsB′_TwinStrep 52.608 kDa, HisTEV_ThsB′ 49.654 kDa, ThsB′ 45.694 kDa, ThsB_TwinStrep 51.783 kDa. **c**, ThsB′ uses NAD^+ or εNAD^+ to produce an isomeric cyclic ADP ribose product. Extracted ion current (EIC) of mass signal corresponding to a cyclic product as well as mass spectra are presented. MS of canonical cADPR is also shown. Shaded peak area represents the analysis time frame of MS spectra shown. ($[M\text{-}H]^-$ theoretical values: NAD^+ 662.1018, cADPR isomer 540.0538, $[M\text{-}H]^+$ theoretical values: εNAD^+ 688.1164, cεADPR isomer 566.0684). All values are presented in detector counts. Data are representative of n = 3 independent experiments. **d**, Tagged and non-tagged ThsB′ forms are able to activate ThsA in a εNAD^+-based fluorescence assay. Data are presented as mean ± s.d. for n = 3 independent experiments, with individual data points overlaid.

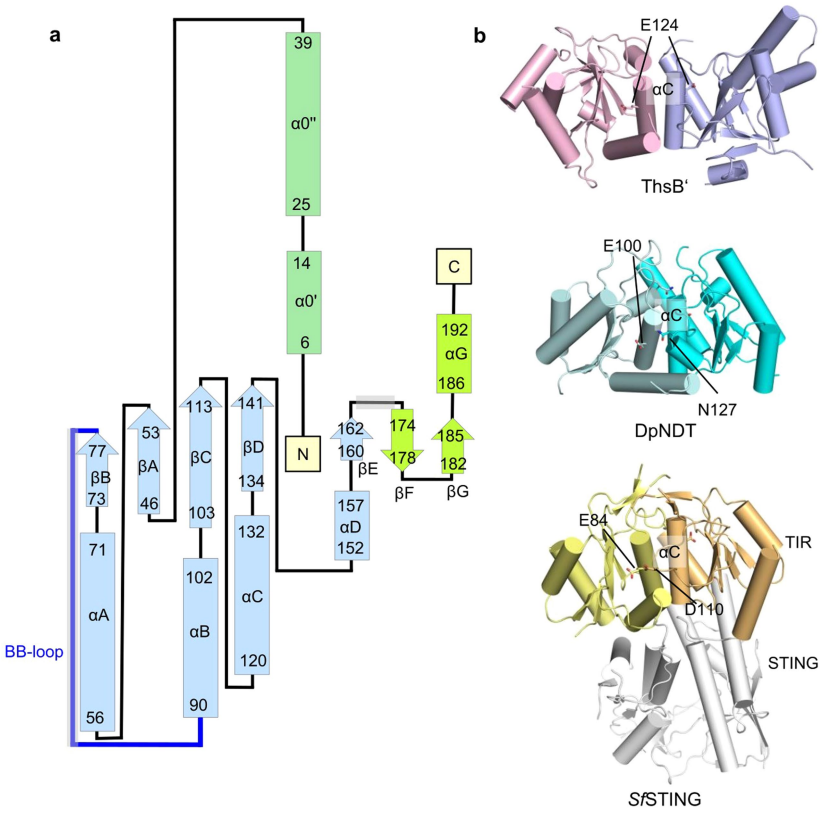

Extended Data Fig. 2 | Crystal structure of ThsB'. a, Topology diagram of ThsB'. Conserved TIR elements are colored light blue, unique ThsB' structural features are colored light green and lime green. BB-loop is shown in blue. Gray boxes mark the loops that are disordered in both subunits of the asymmetric unit. **b**, Comparison of the ThsB' dimer with the dimers of DpNDT (PDB ID 7O62[46]) and *Sf*STING (PDB ID 7UN8[47]). Active site residues and complementing residues from the DD loop of the second subunit of DpNDT and *Sf*STING are shown.

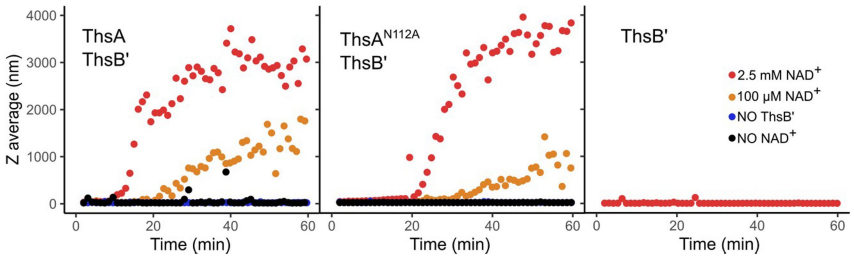

Extended Data Fig. 3 | 1″–3′ gcADPR binding induced polymerization of ThsA in solution. Temporal Dynamic Light Scattering (DLS) analysis of the reaction mixtures containing ThsA and ThsB′ started with NAD^+. Plotted Z average diameter values qualitatively indicate ThsB′ and NAD^+ dependent oligomerization of ThsA into higher order species. Comparison with ThsB′ or NAD^+ reaction control indicates that observed oligomerization is by ThsA and not ThsB′ molecules.

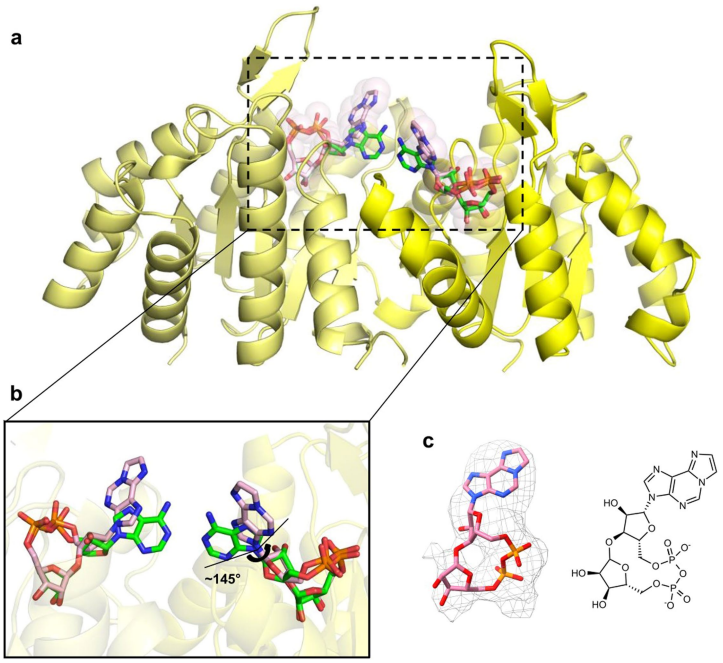

Extended Data Fig. 4 | The ThsA SLOG domain bound to 1″–3′ gcεADPR. **a**, The ThsA SLOG domain dimer, bound to 1″–3′ gcεADPR (pink). 1″–3′ gcADPR (green) is shown for comparison. **b**, Adenine ring is rotated ~145° in 1″–3′ gcεADPR compared to 1″–3′ gcADPR due to a possible steric clash of two bound 1″–3′ gcεADPR. **c**, Local refinement unsharpened electrostatic potential map for 1″–3′ gcεADPR and its chemical formula.

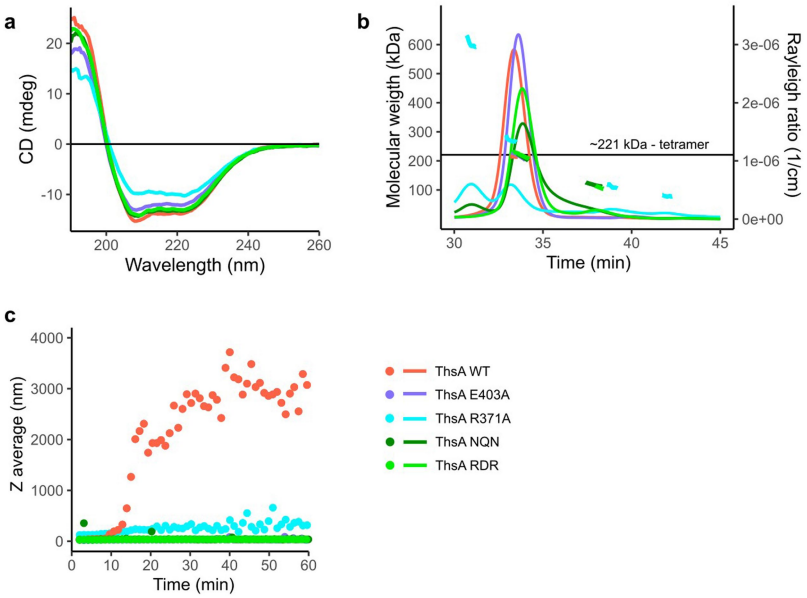

Extended Data Fig. 5 | Characterization of the ThsA mutants. a, CD spectroscopy results of WT and mutant ThsA proteins. Mutant proteins and WT exhibited CD spectra indicative of properly folded proteins. **b**, SEC-MALS analysis of WT and mutant ThsA proteins. Calculated molecular masses of mutant and WT proteins eluting at a single peak indicate tetrameric oligomeric state (ThsA WT monomer theoretical Mw 55.39 kDa). ThsA R371A exhibits polydispersity with multiple elution peaks. **c**, Temporal dynamic light scattering analysis of mutant ThsA proteins activated using ThsB′ and NAD^+.

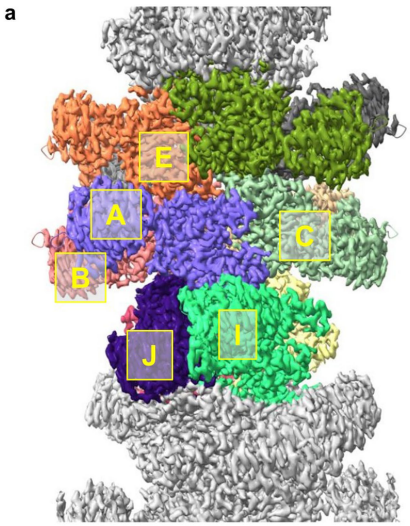

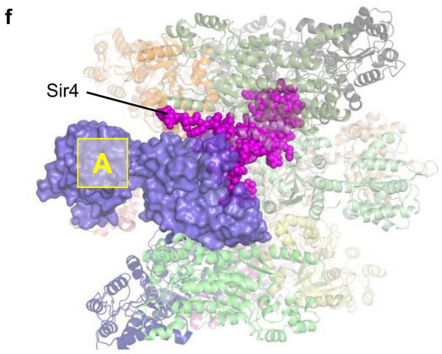

b

##	Subunit A	Dist. [Å]	Other subunit
Tetramer interface A-C (burried area ~1477.9 Å^2)			
1	A:ILE 51[O]	2.69	C:ARG 244[NE]
2	A:ILE 51[O]	2.62	C:ARG 244[NH2]
3	A:ASP 54[N]	3.84	C:TYR 241[OH]
4	A:ASP 54[O]	3.24	C:TYR 241[OH]
5	A:LYS 57[NZ]	3.67	C:ASP 238[OD1]
6	A:GLU 58[OE2]	3.05	C:TYR 241[OH]
7	A:LYS 165[NZ]	3.68	C:ASP 252[OD2]
8	A:ASP 166[OD2]	2.22	C:ARG 211[NH1]
9	A:GLU 169[OE1]	3.88	C:ARG 211[NH1]
10	A:GLU 169[O]	3.15	C:ARG 209[NH1]
11	A:GLU 169[OE1]	2.62	C:ARG 255[NH2]
12	A:ARG 209[NH1]	3.14	C:GLU 169[O]
13	A:ARG 211[NH1]	2.22	C:ASP 166[OD2]
14	A:ARG 211[NH1]	3.88	C:GLU 169[OE1]
15	A:ASP 238[OD1]	3.67	C:LYS 57[NZ]
16	A:TYR 241[OH]	3.84	C:ASP 54[N]
17	A:TYR 241[OH]	3.24	C:ASP 54[O]
18	A:TYR 241[OH]	3.05	C:GLU 58[OE2]
19	A:ARG 244[NE]	2.69	C:ILE 51[O]
20	A:ARG 244[NH2]	2.62	C:ILE 51[O]
21	A:ASP 252[OD2]	3.68	C:LYS 165[NZ]
22	A:ARG 255[NH2]	2.62	C:GLU 169[OE1]
Helical interface A-J (burried area ~798.4 Å^2)			
1	A:GLN 81[OE1]	3.57	J:THR 140[N]
2	A:GLN 81[NE2]	2.80	J:THR 140[O]
3	A:ASP 85[OD1]	3.34	J:VAL 142[N]
4	A:TYR 132[OH]	3.59	J:TYR 132[OH]
5	A:TYR 132[OH]	2.75	J:HIS 157[NE2]
6	A:GLN 136[NE2]	2.76	J:GLU 156[O]
7	A:THR 140[O]	2.78	J:GLN 81[NE2]
8	A:THR 140[N]	3.56	J:GLN 81[OE1]
9	A:LYS 141[NZ]	3.38	J:GLU 156[OE1]
10	A:LYS 141[NZ]	3.38	J:GLU 156[OE2]
11	A:VAL 142[N]	3.31	J:ASP 85[OD1]
12	A:GLU 156[O]	2.76	J:GLN 136[NE2]
13	A:GLU 156[OE1]	3.42	J:LYS 141[NZ]
14	A:GLU 156[OE2]	3.40	J:LYS 141[NZ]
15	A:HIS 157[NE2]	2.77	J:TYR 132[OH]
Helical interface A-E/I-A (burried area ~657.9 Å^2)			
1	A:ASP 13[OD1]	3.42	E:ARG 78[NH1]
2	A:LYS 16[NZ]	3.71	E:ASP 85[OD2]
3	**A:ARG 216[O]**	2.80	E:ARG 76[N]
4	**A:ARG 216[NH2]**	3.90	E:ASP 167[OD1]
5	**A:ARG 216[NH1]**	3.68	E:ASP 167[OD1]
6	**A:ASP 217[OD1]**	2.99	E:ASN 80[ND2]
7	A:ARG 219[NH2]	3.69	E:GLN 81[OE1]
8	**A:ARG 220[NH1]**	2.81	E:GLU 50[OE2]
9	**A:ARG 220[NH2]**	3.05	E:GLU 50[OE2]
10	**A:ARG 220[NH2]**	2.45	E:TYR 68[OH]
11	**A:ARG 220[NH2]**	2.94	**E:ASN 72[OD1]**
12	A:SER 251[OG]	3.07	**E:GLN 73[NE2]**
13	A:SER 254[O]	2.97	**E:ASN 75[ND2]**
14	A:ARG 255[O]	3.44	**E:ASN 75[ND2]**
15	A:LYS 259[NZ]	3.08	E:GLU 50[OE2]

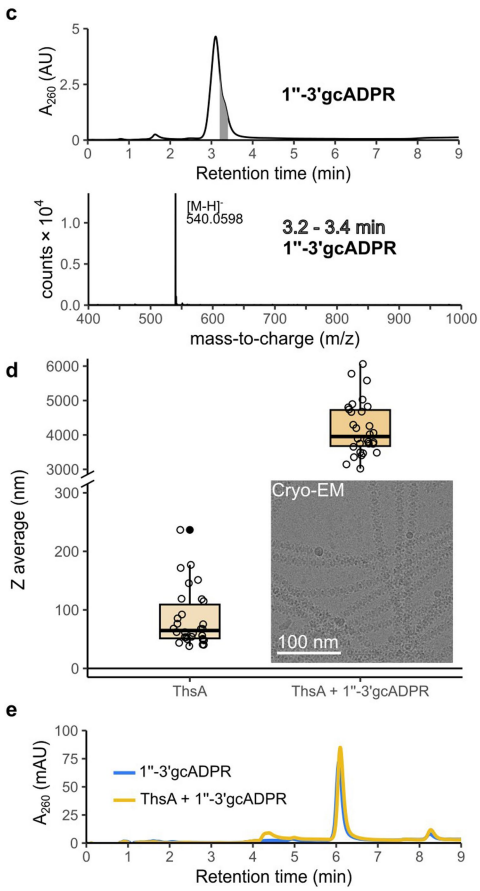

Extended Data Fig. 6 | Structural and biochemical features of the helical filament. a, Cryo-EM map showing 12 subunits in different colors. Each subunit makes contacts with 5 other subunits. Subunit A makes dimerization contacts with subunit B involving both SLOG and SIR2 domains, also makes tetramerization contacts with C subunit and stabilizing helical interactions with E, I and J subunits. Interactions A-E and I-A are symmetric. **b**, List of the residues making hydrogen bonds in the tetramerization and helical interfaces (calculated by PDBePISA[45]). Residues from the elements undergoing conformational changes in SIR2 domain (shown in Fig. 2g) are shown on a light orange background. Helical interface residues NQN are colored magenta, RDR residues are colored blue. **c**, MS of purified 1″–3′ gcADPR used for further experiments. **d**, DLS analysis of ThsA–1″–3′ gcADPR complex. Data are represented as boxplots (n = 30 independent measurements) where the middle line is the median, the lower and upper hinges correspond to the first and third quartiles, the upper whisker extends from the hinge to the largest value no further than 1.5 × IQR from the hinge (where IQR is the inter-quartile range) and the lower whisker extends from the hinge to the smallest value at most 1.5 × IQR of the hinge, while data beyond the end of the whiskers are outlying points that are plotted individually as solid dots. Individual data points are overlaid as open dots. An inlet shows a representative micrograph (n = 600) of ThsA–1″–3′ gcADPR 1:1 complex. **e**, HPCL analysis of 1″–3′ gcADPR after incubation with ThsA. **f**, Structural superposition of yeast Sir2-Sir4 complex (PDB ID 4IAO) with the ThsA A subunit SIR2 domain. Sir2 is omitted for clarity, Sir4 is colored magenta and shown is in sphere representation. ThsA subunits are colored as in (a), the surface of the ThsA A subunit (violet) is shown.

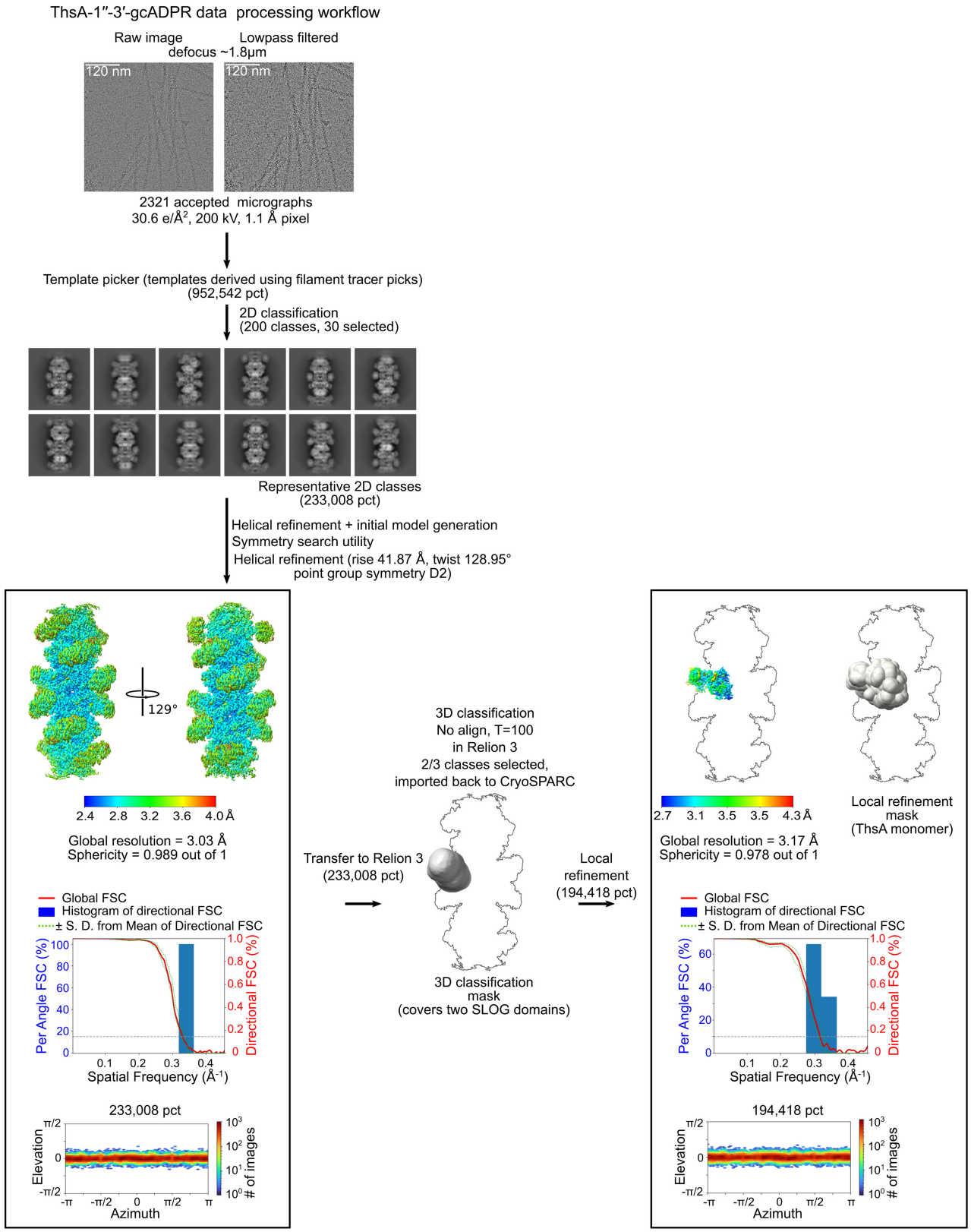

Extended Data Fig. 7 | Cryo-EM helical reconstruction workflow of ThsA-1″–3′ gcADPR complex. The final electron density maps showing local resolution, masks from the local refinement jobs, directional distribution plots and FSC (Fourier shell correlation) plots of helical (left) and local refinement (A subunit, right) are shown in black rectangles.

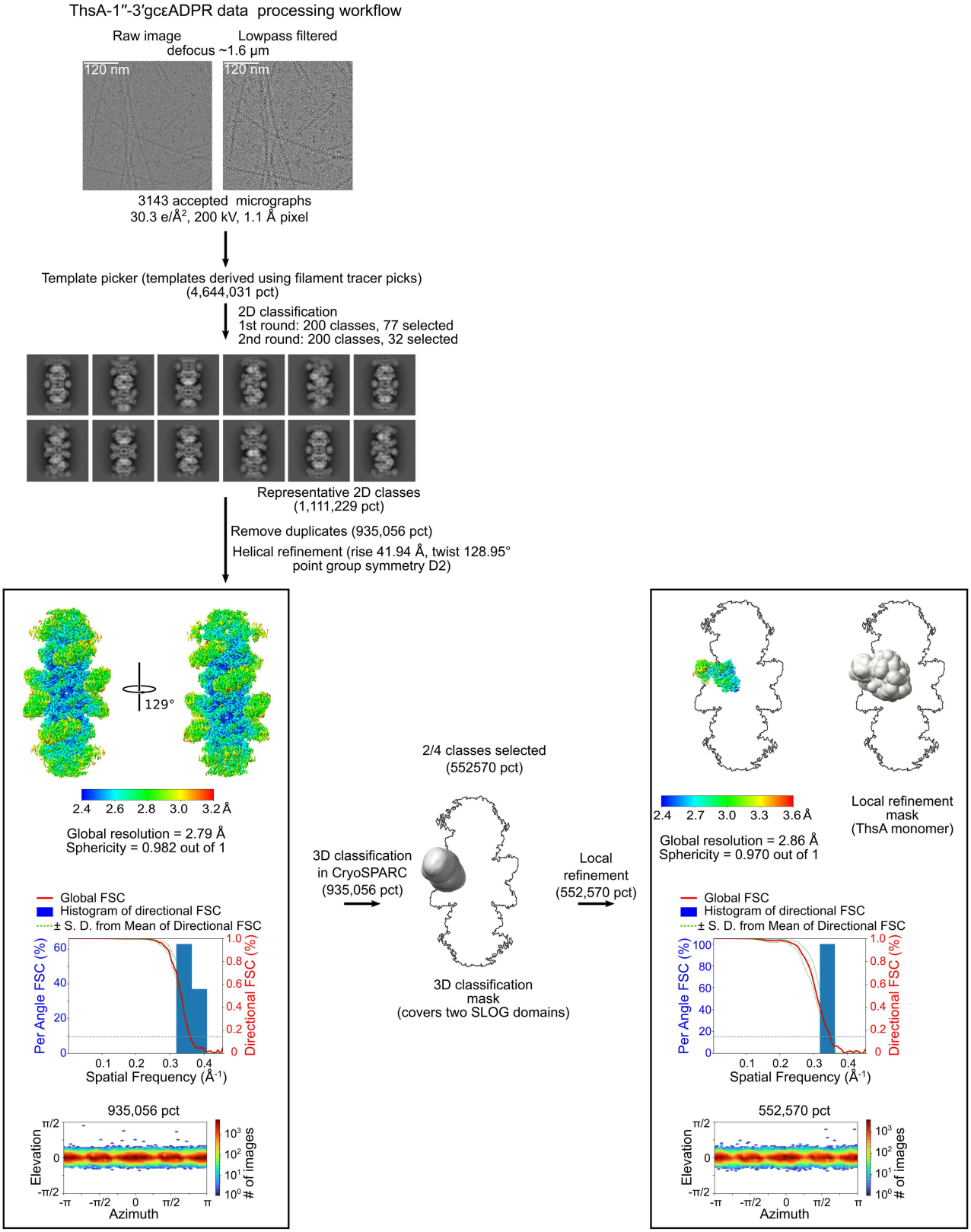

Extended Data Fig. 8 | Cryo-EM helical reconstruction workflow of ThsA-1″–3′ gcεADPR complex. The final electron density maps showing local resolution, masks from the local refinement jobs, directional distribution plots and FSC (Fourier shell correlation) plots of helical (left) and local refinement (A subunit, right) are shown in black rectangles.

Extended Data Table 1 | X-ray data collection and refinement

	BcThsB′ (PDB 8BTN)
Data collection	
Space group	P 2_1 2_1 2_1
Cell dimensions	
a, b, c (Å)	46.18 73.92 125.04
α, β, γ (°)	90 90 90
Resolution (Å)	43.32-3.1 (3.211-3.1)*
R_{merge}	0.096 (0.959)
I / σI	20.23 (2.83)
Completeness (%)	99.74 (100.00)
Redundancy	13.1 (13.5)
Refinement	
Resolution (Å)	43.32-3.1
No. reflections	8200 (790)
R_{work} / R_{free}	0.238/0.265 (0.319/0.320)
No. atoms	
Protein	2637
Ligand/ion	0
Water	0
B-factors	
Protein	79.55
Ligand/ion	-
Water	-
R.m.s. deviations	
Bond lengths (Å)	0.002
Bond angles (°)	0.51

*Values in parentheses are for highest-resolution shell.

Extended Data Table 2 | Cryo-EM data collection and refinement

	ThsA in complex with 1″-3′gcADPR (EMDB-16233) (PDB 8BTO)	ThsA in complex with 1″-3′gcεADPR (EMDB-16234) (PDB 8BTP)
Data collection and processing		
Magnification	92000	92000
Voltage (kV)	200	200
Electron exposure (e–/Å^2)	30.64	30.33
Defocus range (μm)	-1.0/-2.0	-1.0/-2.0
Pixel size (Å)	1.10	1.10
Initial particle images (no.)	952542	4644031
Final particle images (no.)	233008	935056
Map resolution (Å)	3.03	2.79
FSC threshold	0.143	0.143
Map resolution range (Å)	2.48-23.61	2.43-7.82
Refinement		
Initial model used (PDB code)	6LHX	8BTO
Model resolution (Å)	3.0	2.7
FSC threshold	0.143	0.143
Model resolution range (Å)	2.9/3.0/3.1	2.7/2.7/2.9
Map sharpening *B* factor (Å^2)	-165.9	-148.5
Model composition		
Non-hydrogen atoms	46128	46260
Protein residues	5676	5676
Ligands	24	24
B factors (Å^2)		
Protein	102.30	46.57
Ligand	91.73	54.69
R.m.s. deviations		
Bond lengths (Å)	0.007	0.005
Bond angles (°)	0.696	0.678
Validation		
MolProbity score	1.54	1.46
Clashscore	9.79	8.58
Poor rotamers (%)	0.25	0.50
Ramachandran plot		
Favored (%)	97.87	98.67
Allowed (%)	2.13	1.33
Disallowed (%)	0	0

nature portfolio

Corresponding author(s): Giedre Tamulaitiene, Mindaugas Zaremba and Virginijus Siksnys

Last updated by author(s): Sep 15, 2023

Reporting Summary

Nature Portfolio wishes to improve the reproducibility of the work that we publish. This form provides structure for consistency and transparency in reporting. For further information on Nature Portfolio policies, see our Editorial Policies and the Editorial Policy Checklist.

Statistics

For all statistical analyses, confirm that the following items are present in the figure legend, table legend, main text, or Methods section.

n/a	Confirmed
☐	☒ The exact sample size (*n*) for each experimental group/condition, given as a discrete number and unit of measurement
☐	☒ A statement on whether measurements were taken from distinct samples or whether the same sample was measured repeatedly
☒	☐ The statistical test(s) used AND whether they are one- or two-sided *Only common tests should be described solely by name; describe more complex techniques in the Methods section.*
☒	☐ A description of all covariates tested
☒	☐ A description of any assumptions or corrections, such as tests of normality and adjustment for multiple comparisons
☐	☒ A full description of the statistical parameters including central tendency (e.g. means) or other basic estimates (e.g. regression coefficient) AND variation (e.g. standard deviation) or associated estimates of uncertainty (e.g. confidence intervals)
☒	☐ For null hypothesis testing, the test statistic (e.g. *F*, *t*, *r*) with confidence intervals, effect sizes, degrees of freedom and *P* value noted *Give P values as exact values whenever suitable.*
☒	☐ For Bayesian analysis, information on the choice of priors and Markov chain Monte Carlo settings
☒	☐ For hierarchical and complex designs, identification of the appropriate level for tests and full reporting of outcomes
☒	☐ Estimates of effect sizes (e.g. Cohen's *d*, Pearson's *r*), indicating how they were calculated

Our web collection on statistics for biologists contains articles on many of the points above.

Software and code

Policy information about availability of computer code

Data collection	The X-ray data were collected at the EMBL/DESY Petra III P14 beamline using mxCuBE v2 user interface. The cryo-EM data were collected on Glacios microscope. Images were recorded with EPU (v2.14.0). The fluorescence of εNAD+ cleavage reactions was measured in a CLARIOstar Plus microplate reader. CD spectra were recorded using a J-815 CD spectropolarimeter (Jasco) using Spectra Manager (v1.54.03) software. DLS measurements were performed with a Zetasizer μV photometer (Malvern Panalytical) using Zetasizer Software (v6.20). LC-MS analysis was performed using HPLC system 1290 Infinity (Agilent Technologies) coupled to mass analyser 6520 Accurate Mass Q-TOF LC/MS (Agilent Technologies), data acquisition was performed on MassHunter and QTOF Acquisition Software (B.02.01 SP1).
Data analysis	CryoSPARC (v3.4.0), 3DFSC (v3.0), Relion 3, AlphaFold2, Coot (v0.9.8.1), UCSF ChimeraX (v1.3), PyMOL (v.2.3.0), phenix.refine (phenix-1.19.2-4158), phenix.real_space_refine (v.1.19.2-4158), XDS (v. Jan 10, 2022), SCALA (v.3.3.22), TRUNCATE (CCP4 v.7.0.000), Phaser (v. 2.8.3), R (v.4.0.2), Agilent Technologies MassHunter Qualitative Analysis B.05.00, Astra (v.7.3.2.19 64-bit), R (v.4.0.2), PDBePISA.

For manuscripts utilizing custom algorithms or software that are central to the research but not yet described in published literature, software must be made available to editors and reviewers. We strongly encourage code deposition in a community repository (e.g. GitHub). See the Nature Portfolio guidelines for submitting code & software for further information.

Data

Policy information about availability of data

All manuscripts must include a data availability statement. This statement should provide the following information, where applicable:

- Accession codes, unique identifiers, or web links for publicly available datasets
- A description of any restrictions on data availability
- For clinical datasets or third party data, please ensure that the statement adheres to our policy

All data are available in the manuscript and the supplementary material. The atomic coordinates and cryo-EM density maps have been deposited in the Protein Data Bank and Electron Microscopy Data Bank under accession codes 8BTN (ThsB' crystal structure), 8BTO / EMD-16233 (ThsA–1''-3'gcADPR), 8BTP / EMD-16234 (ThsA–1''-3'gcεADPR). Source data are provided with this paper. The crystal structures in Fig. 1e (PDB accession code 6LHY), Fig. 2g and 3a (6LHX), Fig. 2h (1ICI), Extended Fig. 2b (7O62, 7UN8), Extended Fig. 6f (4IAO) are publicly available from Protein Data Bank.

Human research participants

Policy information about studies involving human research participants and Sex and Gender in Research.

Reporting on sex and gender	not applicable
Population characteristics	not applicable
Recruitment	not applicable
Ethics oversight	not applicable

Note that full information on the approval of the study protocol must also be provided in the manuscript.

Field-specific reporting

Please select the one below that is the best fit for your research. If you are not sure, read the appropriate sections before making your selection.

☒ Life sciences ☐ Behavioural & social sciences ☐ Ecological, evolutionary & environmental sciences

For a reference copy of the document with all sections, see nature.com/documents/nr-reporting-summary-flat.pdf

Life sciences study design

All studies must disclose on these points even when the disclosure is negative.

Sample size	No statistical approaches were used to predetermine the sample size. Cryo-EM sample size was determined by the particle density on electron microscopy grids. The sample size was sufficient to obtain structures at the reported resolution, as assessed by Fourier Shell Correlation (cutoff of 0.143). X-ray dataset size was determined by the crystal diffraction resolution. 3-5 independent replicates of biochemical and in vivo experiments were performed.
Data exclusions	Particles were excluded during 2D and 3D reconstruction and model refinement of cryo-EM. Removal of suboptimal particles is standard practice in single-particle cryoEM and is necessary to obtain homogenous and high-resolution reconstructions.
Replication	Reproducibility was ensured by repeating most of the experiments independently at least 3 times, as indicated in the figure legends.
Randomization	Not relevant to this study as there are no animal nor human experiments, and the experimental outcome does not depend on the order in which samples were analyzed in the experiments.
Blinding	Not relevant to this study as there are no animal nor human experiments, and the knowledge of the order or identity of a sample does not change the experimental outcome.

Reporting for specific materials, systems and methods

We require information from authors about some types of materials, experimental systems and methods used in many studies. Here, indicate whether each material, system or method listed is relevant to your study. If you are not sure if a list item applies to your research, read the appropriate section before selecting a response.

Materials & experimental systems

n/a	Involved in the study
☒	☐ Antibodies
☒	☐ Eukaryotic cell lines
☒	☐ Palaeontology and archaeology
☒	☐ Animals and other organisms
☒	☐ Clinical data
☒	☐ Dual use research of concern

Methods

n/a	Involved in the study
☒	☐ ChIP-seq
☒	☐ Flow cytometry
☒	☐ MRI-based neuroimaging